The magnetic resonance shutter speed discriminates vascular properties of malignant and benign breast tumors in vivo

Wei Huang[a,b,c,d], Xin Li[d], Elizabeth A. Morris[b,c], Luminita A. Tudorica[d,e,f,g], Venkatraman E. Seshan[h], William D. Rooney[d], Ian Tagge[d], Ya Wang[a], Jingang Xu[d], and Charles S. Springer, Jr.[d,g,i,j,1]

Departments of [a]Medical Physics and [b]Radiology, Memorial Sloan-Kettering Cancer Center, New York, NY 10021; [c]Department of Radiology, Weill Medical College, Cornell University, New York, NY 10021; [d]W. M. Keck Foundation High-Field MRI Laboratory-Advanced Imaging Research Center, [g]Knight Cancer Institute, and Departments of [i]Physiology and Pharmacology, [j]Biomedical Engineering, and [f]Radiology, Oregon Health and Science University, Portland, OR 97239; [e]Department of Radiology, State University of New York, Stony Brook, NY 11794; and [h]Department of Biostatistics, Columbia University, New York, NY 10032

Edited by Alexander Pines, University of California, Berkeley, CA, and approved July 17, 2008 (received for review December 3, 2007)

The pharmacokinetic analysis of dynamic-contrast-enhanced (DCE) MRI data yields K^{trans} and k_{ep}, two parameters independently measuring the capillary wall contrast reagent transfer rate. The almost universally used standard model (SM) embeds the implicit assumption that equilibrium transcytolemmal water exchange is effectively infinitely fast. In analyses of routine DCE-MRI data from 22 patients with suspicious breast lesions initially ruled positive by institutional screening protocols, the SM K^{trans} values for benign and malignant lesions exhibit considerable overlap. A form of the shutter-speed model (SSM), which allows for finite exchange kinetics, agrees with the SM K^{trans} value for each of the 15 benign lesions. However, it reveals that the SM underestimates K^{trans} for each of the seven malignant tumors in this population. The fact that this phenomenon is unique to malignant tumors allows their complete discrimination from the benign lesions, as validated by comparison with gold-standard pathology analyses of subsequent biopsy tissue samples. Likewise, the SM overestimates k_{ep}, particularly for the benign tumors. Thus, incorporation of the SSM into the screening protocols would have precluded all 68% of the biopsy/pathology procedures that yielded benign findings. The SM/SSM difference is well understood from molecular first principles.

cancer | water exchange | MRI | screening | DCE

Screening for breast cancer represents one of modern medicine's success stories. However, the continued large fraction of false positives in current diagnostic protocols (1) often leads to biopsy/pathology procedures that append considerable pain, anxiety, healthcare cost, and possibly increased malignancy risk, but that are potentially avoidable. To address this problem, there have been recent calls for the increased use of magnetic resonance imaging (MRI) in breast screening (2, 3).

Early in the development of medical MRI, it was realized that hydrophilic paramagnetic molecules could enhance image contrast, and that the shape of the water proton (^1H_2O) signal intensity time course after a bolus injection of such a contrast reagent (CR) contained considerable patho-physiological information, promising even possible quantitative vascular phenotyping.

Major efforts have been mounted for the pharmacokinetic analyses of such time-course data (4). It was natural that mathematical models for these were taken from the field of nuclear medicine, where such algorithms have matured. However, these were developed for tracer pharmacokinetics, with the intrinsic feature of direct radiotracer detection. Although the MRI CR plays the tracer role, the signal molecule remains water: the CR is detected only indirectly, via its effect on the nature of tissue ^1H_2O relaxation. Affecting the recovery of longitudinal ^1H_2O magnetization (i.e., in the magnetic field direction) requires (transient) water CR molecular interaction, as depicted in Fig. 1. The three major loci for tissue water, the cytoplasmae, the interstitium, and the blood, are indicated in Fig. 1 by subscripts i, o (or e), and b (p, for plasma), respectively. There are water-binding equilibria depicted in each compartment in which the CR is thought to enter. The compartmental volume fractions are designated as v_i, v_e, and v_b, respectively, although the relative areas in Fig. 1 are not proportional.

The CR and water molecules are never equally distributed in tissue. Therefore, the only way that most water (cytoplasmic) can access CR is via exchange equilibria across cytolemmae and blood vessel walls. These are indicated in Fig. 1 with the unidirectional rate constants, k_{oi}, k_{io} and k_{po}, k_{op}, respectively. Initially, the tracer pharmacokinetic models were applied directly to MRI data (4); we refer to these as the standard model (SM) family. Inadvertently, however, this derivation results in the constraint that all intercompartmental equilibrium water exchange processes be treated as if infinitely fast ($k_{oi} + k_{io} \to \infty$ and $k_{po} + k_{op} \to \infty$). This corollary is not valid (5, 6), and its assumption can effectively "short circuit" MRI determination of CR compartmentalization (5, 7), the pharmacokinetic essence. In a series of papers (5, 6, 8–18), we have examined the significance of this implication. We refer to the incorporation of equilibrium water exchange MR effects into the pharmacokinetic derivation as yielding the shutter-speed model (SSM) family.

In dynamic-contrast-enhanced (DCE) MRI, monomeric Gd(III) chelate CRs can increase longitudinal ^1H_2O relaxation rate constant R_1 [$\equiv (T_1)^{-1}$] values, and therefore T_1-weighted signal intensities, during the CR bolus passage through the field of view. Breast cancer screening has been a major thrust for DCE-MRI (19–22), particularly because of the angiogenic nature of the tumors (20, 23). At least because of its greater sensitivity compared with other modalities, the recent advocacy for increased MRI breast screening favors DCE-MRI (2, 3). Disappointingly, though, SM DCE-MRI has not exhibited sufficiently increased specificity to reinforce this advocacy and become widely incorporated into standard clinical protocols, between mammography (which, although relatively inexpensive, suffers a high false positive rate) and biopsy/pathology, with the detriments listed above. Absent good specificity, DCE-MRI will not be cost effective relative to biopsy/pathology (2, 24), because both procedures will still be often necessary.

A preliminary study of a small, six patient cohort suggested that SSM analyses of breast cancer DCE-MRI data could improve specificity compared with SM findings (14). Here, we report that, with an expanded population (22 patients) for whom the institu-

Author contributions: W.H., E.A.M., L.A.T., and C.S.S. designed research; W.H., E.A.M., and L.A.T. performed research; W.H., X.L., V.E.S., I.T., Y.W., J.X., and C.S.S. analyzed data; and W.H., X.L., W.D.R., and C.S.S. wrote the paper.

The authors declare no conflict of interest.

This article is a PNAS Direct Submission.

Freely available online through the PNAS open access option.

[1]To whom correspondence should be addressed. E-mail: springer@ohsu.edu.

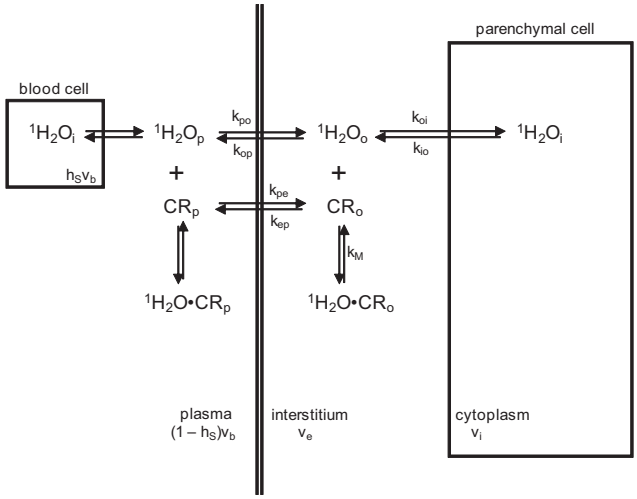

Fig. 1. A cartoon depiction of aspects of pharmacokinetic modeling for DCE-MRI. The three general compartments for CR and water (blood, interstitium, and parenchymal cytoplasmic) are drawn, although not in relative proportions to their volume fractions (v_b, v_e, and v_i). The pertinent chemical equilibria and their unidirectional rate constants are indicated.

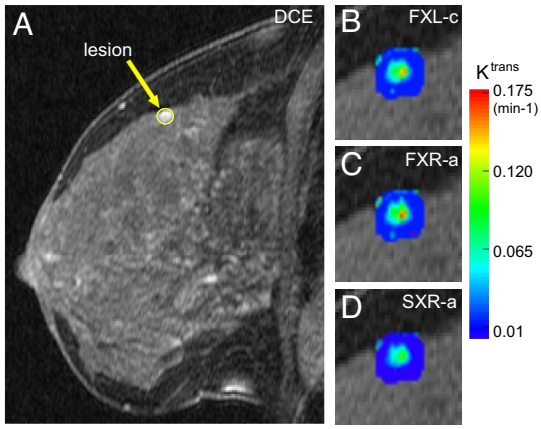

Fig. 2. Breast MR images. (*A*) A sagittal, fat-suppressed breast DCE-MRI image containing a malignant IDC tumor (circled contrast-enhanced region-of-interest) is shown. (*B–D*) Pharmacokinetic K^{trans} parametric maps of the tumor, generated by the SM (FXL-c) (*B*) and two members of the SSM family (FXR-a; *C*) and (SXR-a; *D*), are shown. (Magnification: ×2.5; *B*, *C*, and *D* relative to *A*.)

tional protocols (mammography and/or routine clinical MRI) yielded a positive predictive value (PPV) of only 32% (as proven by subsequent biopsy) and SM DCE-MRI yields at best 54% (maintaining 100% sensitivity; i.e., all malignant lesions identified), the SSM analyses achieve 100% PPV. Moreover, this success is accomplished with even region-of-interest (ROI) data from common clinical acquisitions yielding relatively poor image signal/noise ratios and truncated pharmacokinetic periods.

Results

MRI Data. Data were obtained with consent from patients with positive mammographic and/or clinical MRI reports from standard, institutional breast cancer work-ups and protocols. All had MRI contrast-enhanced lesions radiologically classified as BI-RADS (Breast Imaging Reporting and Data System) four (B-4, suspicious) or five (B-5, highly suggestive of malignancy) (see *Materials and Methods*). Emphasizing practicability and robustness, the data are of a rather routine clinical nature (and they were obtained at two different institutions, with two different instruments, CRs, etc.). The two different data acquisitions were by no means optimized for DCE-MRI. For example, although the spatial resolution is reasonable, the temporal resolution is not optimal. Of particular interest is the fact that the adipose tissue -^1H_2C- MR signal was suppressed in the acquisitions at one institution, whereas at the other institution it was not.

Fig. 2*A* shows the DCE pharmacokinetic image of sagittal slice 16 (numbering from lateral to medial) of the left breast of a 52-year-old patient, obtained 2.6 min after CR injection. It was acquired with adipose –^1H_2C– suppression (required in the institutional protocol). In contrast to those (14, 15) with no fat suppression, this darker image shows glandular regions brighter than fatty tissue. The ROI circumscribes the enhanced lesion evident on the superior edge of normal glandular tissue in this slice, subsequently found to be a malignant invasive ductal carcinoma (IDC) by pathology analysis. Each of the 22 patients participated in a DCE-MRI acquisition subsequent to her clinical mammography and/or MRI screening but before the biopsy procedure and the pathology analysis.

Comparison of Pharmacokinetic Model and Gold-Standard Pathology Analyses. The DCE-MRI acquisition details are given in ref. 18. For each of the 22 subjects, we analyzed ROI DCE time-course data from one sagittal image slice (of 16–40 per breast) that exhibited a lesion to be subsequently biopsied. An ROI boundary was manually drawn around the entire lesion in a pharmacokinetic image showing near maximal enhancement (as in Fig. 2*A*). The patients are enumerated in Table 1 (the Fig. 2 images are from patient 3). The DCE-MRI time courses were each analyzed with several pharmacokinetic models. Considerable detail is given in ref. 18. The 4- to 7 min time-course data and model fittings for several of the subjects have been reported (patients 4 and 8, figure 1 of ref. 18; patients 5 and 20, figure 1 of ref. 14; and patient 6, figure 1 of ref. 15).

For the results presented here, ROI boundaries around each lesion were separately drawn by each of two independent investigators (W.H. and I.T.) who were blinded to the pathology results. The analyses of these ROI data were also conducted independently by the two investigators. The algebraic means of the model parameters returned from each investigator's fitting were computed lesion-by-lesion.

The results of fittings with two different models are presented here. Each of these neglects the small blood water proton signal ($^1H_2O_b$), thus, these are "first-generation" versions (5). For this situation, the MR exchange system of interest is that for equilibrium transcytolemmal water interchange (k_{oi} and k_{io}; Fig. 1). The system's condition is given by the comparison of the equilibrium kinetics, $k = k_{oi} + k_{io}$, with the pertinent MR shutter speed, $\tau^{-1} \equiv |R_{1o} - R_{1i}|$, where R_{1o} and R_{1i} are the relaxation rate constants for the $^1H_2O_o$ and $^1H_2O_i$ signals, respectively, in the absence of exchange. Before CR arrival, $R_{1o} \approx R_{1i}$ and $\tau^{-1} \ll k$. Although k is finite, and invariant throughout the DCE-MRI study, the system is in the fast-exchange limit (FXL): the kinetics appear infinitely fast, and the measured tissue ^1H_2O R_1 is single-valued. As stated above, the SM assumes that the system remains in the FXL throughout the CR bolus passage, so we refer to it also as the FXL-constrained (FXL-c) model. However, as the CR_o concentration increases, R_{1o} becomes increasingly larger than R_{1i} and τ^{-1} can at least approach the constant k value. For some period, the measured R_1 remains effectively single-valued, and we have defined this to be the fast-exchange regime (FXR) (5, 8). The SSM that admits departure from the FXL for the FXR is referred to as FXR-allowed (FXR-a) (12). Further CR_o increase can lead to the condition where R_1 is effectively double-valued: we refer to this as the slow-exchange regime (SXR) (5, 8). The SSM that admits discernable R_1 double-valuedness is referred to as SXR-allowed (SXR-a) (12). For the cases here, the results of FXL-c and FXR-a

Table 1. FXL-c and FXR-a analyses

Patient no.	BIRADS	K^{trans}, min^{-1} SM, FXL-c	K^{trans}, min^{-1} SSM, FXR-a	k_{ep}, min^{-1} SM, FXL-c	k_{ep}, min^{-1} SSM, FXR-a	Pathology report
1	B-4	0.073	0.147	0.389	0.249	DCIS, intermediate nuclear grade
2	B-4	0.110	0.180	0.452	0.447	IDC, histologic grade II/III; DCIS, intermediate nuclear grade; DCIS $\leq$ 25% of total tumor mass.
3	B-4	0.087	0.131	0.161	0.147	IDC present at the edge of the core
4	B-5	0.164 ($\pm$ 0.028)	0.254 ($\pm$ 0.029)	0.532	0.432	IDC, histologic grade II/III; DCIS, intermediate nuclear grade; DCIS > 25% of total tumor mass.
5	B-5	0.559 ($\pm$ 0.040)	1.63 ($\pm$ 0.06)	1.795	2.966	IDC, histologic grade II/III
6	B-5	0.145	0.185 ($\pm$ 0.020)	0.506	0.308	IDC
7	B-4	0.051	0.081	0.269	0.202	IDC, nuclear grade II, LCIS; moderately differentiated IDC embedded within a larger benign LCIS
8	B-5	0.033 ($\pm$ 0.005)	0.034 ($\pm$ 0.006)	0.106	0.053	LCIS, SF
9	B-4	0.022	0.023	0.147	0.047	FC
10	B-4	0.051	0.058	0.306	0.155	FC
11	B-4	0.040	0.055	0.280	0.120	FC
12	B-4	0.062	0.077	0.397	0.188	Sclerosed papillary lesion, LCIS
13	B-4	0.027	0.028	0.048	0.039	FC
14	B-4	0.030	0.034	0.229	0.096	ADH, SF
15	B-4	0.091	0.099	0.189	0.131	LCIS, SF, FC
16	B-4	0.078	0.087	0.188	0.130	LCIS, ADH
17	B-4	0.108	0.125	0.289	0.166	duct *ectasia*, ADH
18	B-4	0.060	0.066	0.133	0.090	SF, sclerosing adenosis
19	B-4	0.048	0.050	0.185	0.086	FA
20	B-4	0.026 ($\pm$ 0.010)	0.028 ($\pm$ 0.005)	0.174	0.066	FA
21	B-5	0.020	0.022	0.307	0.136	FA
22	B-4	0.016	0.016	0.436	0.078	FA

IDC, invasive ductal carcinoma; DCIS, ductal carcinoma *in situ*; LCIS, lobular carcinoma *in situ*; SF, stromal fibrosis; FC, fibrocystic changes; ADH, atypical ductal hyperplasia; FA, fibroadenoma.

analyses are presented in Table 1. Careful analyses with the SXR-a model suggest that it is incompatible with these data (18); an example will be seen below. There are a number of potentially variable parameters (5, 15). For the SM (FXL-c) analyses, the variables were K^{trans} and v_e, whereas for the SSM (FXR-a) analyses, τ_i was also varied (18). In terms of Fig. 1 notations, $K^{trans} = v_e k_{ep} = v_b k_{pe}$ (4) and $\tau_i = k_{io}^{-1}$. The values returned for K^{trans}, a measure of the rate of passive CR transfer across the vessel wall, and k_{ep}, the unidirectional rate constant for CR intravasation (Fig. 1) are given in Table 1. Sample SD measures of parameter uncertainty from individual fittings are given for some entries. These were determined by multiple Monte Carlo fitting calculations (12, 18). The values for the other parameters varied are presented in ref. 18. In general, the K^{trans} and k_{ep} values for the malignant tumors (first seven entries in Table 1) are larger than those for the benign lesions.

Table 1 indicates that the SM does not completely separate the malignant tumors (first seven entries) from the benign lesions with either the K^{trans} or k_{ep} parameters. However, the SSM increases K^{trans} for every one of the malignant lesions and for none of the benign tumors. Furthermore, although the SSM reduces k_{ep} for both malignant and benign lesions, these reductions are greater for the benign tumors. We will see that these changes allow complete discrimination with the SSM results.

Although neither of the parameters allows the construction of perfect receiver operator characteristic (ROC) plots, the SSM K^{trans} and k_{ep} quantities come very close. Early versions of the K^{trans} ROC plots can be seen in a preliminary report (25).

These aspects are better seen in the 2D parametric scatter plots (26) of the K^{trans} (ordinate) and k_{ep} (abscissa) values presented in Fig. 3. The ROI values for lesions found by pathology analyses (Table 1) to be solely benign are indicated in Fig. 3 by red triangles, and those with major malignant regions are shown as black circles. (The two red circles with black cores in Fig. 3 also represent malignant tumors and will be discussed below.) The results from the SM (FXL-c) analyses are seen in Fig. 3*A*, and those from the SSM (FXR-a) determinations are shown in Fig. 3*B*. The values for patient 5 are so large that they are shown in Fig. 3 *Insets*, which are also marked a and b.

In comparing Fig. 3 *A* and *B*, one can note especially the upward movement (increasing K^{trans}) of the black circles and the leftward movement (decreasing k_{ep}) of the red triangles, in going from the

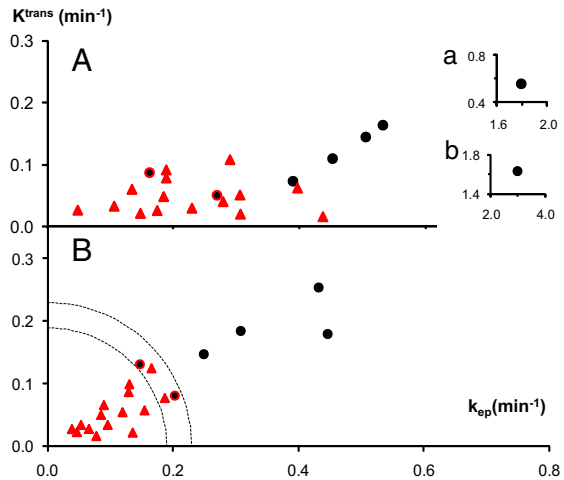

Fig. 3. The 2D scatter plots of the SM (*A*) and SSM (FXR-a) (*B*) results from Table 1 are given. The ordinates measure the K^{trans}, and the abscissae measure the k_{ep} parameters. The black circles mark the positions for ROIs of lesions that were found to have large malignant fractions, and the red triangles are those for lesions found to be solely benign. (*Insets*) An outlier (Table 1, patient 5) is plotted. Dashed concentric quarter-circles are drawn with radii of 0.19 and 0.23 min^{-1}. The points for two patients (3 and 7) are marked as red circles with black cores. These represent lesions with only very small malignant fractions.

SM to the SSM. These shifts allow the almost complete separation of these points in Fig. 3*B*, which is not achieved in any single dimension. The rather tight clustering of the red triangles in Fig. 3*B* is quite interesting. It is important to note that two of the triangles represent B-5 lesions (Table 1): i.e., they were "highly suggestive" false positives. Retaining 100% sensitivity (not missing any malignant tumor), the PPV values for the SM K^{trans}, SM k_{ep}, SSM K^{trans}, and SSM k_{ep} dimensions are: 54%, 39%, 70%, and 70%, respectively. In the Fig. 3*B* SSM 2D plot, one can draw a dashed quarter-circle of radius $([(K^{trans})^2 + (k_{ep})^2]^{1/2})$ 0.19 min^{-1} that also allows a 78% PPV, when used as a binary classifier.

Furthermore, consider the annular region between this and the other concentric quarter-circle of radius 0.23 min^{-1}. The only two malignant tumors (Fig. 3, red circles with black cores) within are those of patients 3 (upper) and 7 (lower). These are cases where the malignant areas are quite small compared with the total tumor area visualized in the biopsy specimen (Table 1), which means that the analyses of whole-tumor ROI-averaged data causes a partial volume dilution of the DCE-MRI parametric values. This diminution can be seen clearly in Fig. 2 *B* and *C*, which presents K^{trans} parametric maps of the lesion of patient 3. In the SM (FXL-c) and SSM (FXR-a) maps (Fig. 2 *B* and *C*, respectively), a clear "hot spot" is seen on the posterior lesion edge. The hot spot has K^{trans} values >0.16 min^{-1} in the FXR-a map, considerably elevated above the ROI-averaged magnitude (Table 1). Likewise, the FXR-a K^{trans} map of the lesion of patient 7 has been reported (figure 2m of ref. 14). It shows two tiny hot spots with K^{trans} values >0.1 min^{-1}. In fact, this ROI is the only one in this population for which the pathology analysis returned a particular malignant/benign result: a moderately differentiated malignant IDC embedded within a larger benign lobular carcinoma *in situ* (LCIS) (Table 1). If an ROI is retrospectively defined as only the malignant IDC core, the point moves upward in Fig. 3 (data not shown). This result may suggest a potential for SSM DCE-MRI staging: might it be that this B-4 patient was imaged quite soon after transformation? Although LCIS has not been generally viewed as a true precursor lesion, recent epidemiological evidence suggests that perhaps it should be, although usually for invasive lobular carcinoma (2, 27).

The hot regions of all seven malignant tumors in this population have SSM K^{trans} values >0.1 min^{-1}. Except for that of patient 17 [upper triangle in Fig. 3*B*, and which uniquely exhibits ductal dilation (Table 1)], 0.1 min^{-1} exceeds the ROI-averaged SSM K^{trans} values of any of the 15 benign lesions. With Fig. 2 *B–D*, parametric maps of four of the seven malignant tumors have now been presented (14, 15). Some hot spots can be as small as 2 mm in diameter (14, 15). In another indication of potential staging power, a plot (data not shown) of "hotness" vs. area of the SSM K^{trans} hot spots in the malignant tumors of patients 5–7 demonstrates that these two independently measured quantities are very highly positively correlated. The fact that the SXR-a K^{trans} map of the patient 3 lesion (Fig. 2*D*) does not show increased values relative to the FXL-c map (Fig. 2*B*), and in fact obliterates the hot spot, is an example of the SXR-a model incompatibility with these data (18). [For the mappings in Fig. 2 *C* and *D*, the τ_i parameter was held fixed at 400 ms (18).]

The K^{trans} and k_{ep} values are rather well correlated in Fig. 3, particularly in Fig. 3*B*. The positions of the Fig. 3 *Insets* are placed with constant coordinate aspect ratios. Thus, one can visually include the inset points in the correlations. The slope of a line drawn through the points represents the mean v_e value of these lesions. Such a line for Fig. 3*B* has a slope near 0.5. The v_e magnitudes for these lesions are discussed extensively in ref. 18.

Discussion

These results suggest a potential breast cancer screening protocol. The first step would be a clinical examination and/or mammography. A positive result (B-4 or B-5), or suspicion of a mammographically occult lesion, would occasion referral for diagnostic MRI that includes DCE. The radiologist can easily circumscribe an ROI from the DCE image showing the greatest enhancement. Alternatively, this process can be automated (ex., Jim 4.0 software; Xinapse Systems). The computer can very quickly (few seconds) conduct SM and SSM analyses on the mean ROI signal time-course data and produce SSM K^{trans} and k_{ep} values, which can be compared with 2D scatter plots such as those in Fig. 3*B*. If a patient's point turns out to be in the annulus between the quarter-circles in Fig. 3*B*, the radiologist could proceed to read K^{trans} parametric lesion maps made from the same DCR-MRI data, although they require more computational time. Hot spots >0.1 min^{-1} would be very suspicious for malignancy.

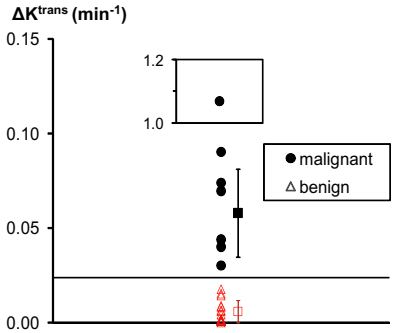

Fig. 4. This 1D scatter plot is derived from Table 1. The ordinate, ΔK^{trans}, is K^{trans}(SSM) − K^{trans}(SM): SSM is FXR-a and SM is FXL-c. The values for the lesion ROIs of all 22 subjects are shown. Those proven malignant are given as filled black circles (these include the two Fig. 3 red circles with black cores), and those found solely benign are indicated by open red triangles. The group mean ΔK^{trans} values are indicated by red and black squares on the right. The error bars represent SD values within each category. (*Inset*) One malignant lesion outlier is plotted and is excluded from the SD calculation. The horizontal cut-off line drawn at 0.024 min^{-1} cleanly separates the two lesion groups.

Some oncologists advocate a separate regimen for a malignant ductal carcinoma *in situ* (DCIS) tumor, possibly simply following it instead of immediate surgery (1), whereas others urge excision (28). The only solely DCIS case in our population is that of patient 1. Her position in Fig. 3*B* is the black point closest to the outer quarter-circle. In fact, another concentric quarter-circle of radius 0.3 min^{-1} would isolate this point. Its position could be "followed," to see whether it moves out along the correlation. [At least qualitative DCE-MRI is required for reliable DCIS detection (28).] Inside the inner quarter-circle, most of the benign LCIS lesions are found in the upper right sector, whereas all of the fibroadenoma lesions are found near the bottom. In the analyses so far, we have been using pseudo-absolute parameter values. The SSM success suggests that neglect of equilibrium transcytolemmal water exchange effects may constitute the most significant systematic error in SM DCE-MRI pharmacokinetic analyses. However, there are surely still smaller systematic errors and random errors. In this context, it is important to note that the results here were obtained by analyses of rather routine clinical DCE-MRI data. In *Room for Improvement*, we list seven specific steps not used here that could be taken, even in the clinical setting, and should improve the precision, possibly the accuracy, and the diagnostic richness of the SSM DCE-MRI pharmacokinetic parameters. These would be expected to mostly decrease the random error scatter in the Fig. 3 point clusters and may allow further discrimination of pathology subtypes.

The NMR Shutter-Speed Effect on K^{trans} Determination. For screening purposes, the most striking aspect of the results in Table 1 and Fig. 3 is that every one of the malignant tumor ROI K^{trans} values (Fig. 3, black circles) is clearly decreased by the SM analysis, whereas every one of the benign lesion ROI values (Fig. 3, red triangles) is not. This result is seen even more clearly in Fig. 4, which presents

the 1D scatter plot for ΔK^{trans} [$\equiv K^{trans}$(SSM) $- K^{trans}$(SM)]. There is a gap between all seven of the black circles (including the two red circles with black cores) [group mean, 0.06 min^{-1} (excluding the inset point)] and all 15 of the red triangles in Fig. 3. The latter set clusters very near zero (group mean, 0.006 min^{-1}). A clean cut-off line is drawn at 0.024 min^{-1}. Because the only difference between these two models is the allowance for the effect on the NMR signal of finite equilibrium transcytolemmal water exchange kinetics, the NMR shutter-speed effect, our finding suggests that the latter is significant (for the K^{trans} magnitude) with the capillary wall permeability obtaining for the vascular beds of only malignant breast tumors. Thus, it is very encouraging that analyses of DCE-MRI ROI data first with one pharmacokinetic model and then with the other (which is still accomplished in only seconds) can lead to extremely high specificity in breast cancer screening. Here, the positive criterion of $\Delta K^{trans} > 0.025$ min^{-1} (ΔK^{trans} as binary classifier) yields 100% PPV.

Molecular Aspects. Apparently, in the vascular beds of only malignant breast tumors does the interstitial ("outside") CR concentration [CR_o] transiently rise to sufficient values during the bolus passage that the equilibrium transcytolemmal water exchange system transiently departs the FXL to sufficient extent and/or for sufficient duration to substantially invalidate the SM K^{trans} determination. The SSM interpretation is that, during the bolus passage through malignant lesions, the relaxographic τ^{-1} value for the transcytolemmal water exchange process, $|R_{1o} - R_{1i}|$, transiently approaches or exceeds that for the unchanging exchange rate constant, $k_{io} + k_{oi}$ (in vivo studies are isothermal), sufficiently for the system to enter at least the FXR, but probably not also the SXR (18). (R_{1o} increases with [CR_o], whereas R_{1i} remains constant.) This phenomenon is a manifestation of the varying equilibrium competition for interstitial water molecules between diamagnetic cytoplasmic spaces and paramagnetic interstitial CR molecules (Fig. 1). Informative estimates can be made:

$$H_2OCR_o \underset{([CR_o]/[H_2O_o])\tau_M^{-1}}{\rightleftharpoons} CR_o + H_2O_o \underset{(v_e^{-1}-1)\tau_i^{-1}}{\rightleftharpoons} H_2O_i$$

in comparison with Table 1 patients 8/4 benign/malignant lesion pair (with SSM K^{trans} 0.034 and 0.254 min^{-1}, respectively). For one of the SSM (FXR-a) fittings of each, the (v_e, τ_i) parameters returned are similar: (0.60, 0.40 s) and (0.69, 0.39 s) for benign and malignant, respectively. Thus, the unidirectional rate constants for water cellular entry [$k_{oi} \approx (v_e^{-1} - 1)\tau_i^{-1}$] are similar (1.7 and 1.2 s^{-1}, respectively), constant, and not infinitely large. However, before the arrival of interstitial CR_o, the transcytolemmal water exchange appears infinitely fast in the NMR signal because τ^{-1} is almost negligible. The interstitial water molecules encounter no paramagnetic CR_o molecules before entering a diamagnetic cytoplasm. However, as [CR_o] increases, the rate constant for interstitial water CR encounter, $([CR_o]/[H_2O_o])\tau_M{}^{-1}$, also increases ($\tau_M{}^{-1} = k_M$ in Fig. 1). Although for the benign lesion [CR_o] maximizes at 0.52 mM (at ≈7.5 min), it is 1.6 mM (at ≈3.5 min) for the malignant tumor. Thus, $([CR_o]_{max}/[H_2O_o])\tau_M{}^{-1}$ values are 104 and 313 s^{-1} for the benign and malignant lesions, respectively (we took the interstitial water concentration [H_2O_o] as 50 M, and the mean water lifetime on the CR, τ_M, as 10^{-7} s). At maximum CR_o, an interstitial water molecule in the benign lesion encounters a paramagnetic CR molecule on average 60 times (104/1.7) before it enters a diamagnetic cell (sufficient, apparently, for the SM 40% v_e underestimation), whereas in the malignant tumor, it happens 260 times (313/1.2) on average, more than four times as often. This branching ratio appears sufficient to cause significant K^{trans} underestimations if it is neglected.

Room for Improvement. It is important to note that the results were obtained by analyses of rather routine clinical DCE-MRI data. In this section, we list seven specific steps not used here that could be taken, even in the clinical setting, and should improve the precision, and possibly the accuracy, and the diagnostic richness of the SSM DCE-MRI pharmacokinetic parameters. These would be expected to mostly decrease the random error scatter in the point clusters in Figs. 3 and 4, which may allow further discrimination of pathology subtypes.

- The DCE-MRI time-course acquisitions, prescribed for radiological considerations, were truncated. Increasing this period would be particularly important for accuracy and precision of the benign lesion parameters. For these ROIs, the maximum R_1 value is seldom reached in the no more than 7 min usually allowed (14, 18). We suspect this truncation is the source of abnormally large v_e values for some benign tumors. Increasing the period to 15 min could considerably help define the shape of the time course, even for the malignant tumors (14, 15, 18).
- The DCE-MRI acquisitions for these data were not particularly exchange sensitive (18). Even so, exchange effects seem to facilitate very high discrimination of malignant from benign breast tumors. In recent years, there has been considerable effort devoted to decreasing the exchange sensitivity of DCE-MRI pulse sequences (29). It seems that there could be significant profit, not the least for cancer screening, in working to actually increase exchange sensitivity. The studies presented in ref. 18 can serve as guides for such endeavors. For example, a slightly larger echo time value may further improve specificity.
- The tissue R_{10} values (the pre-CR ^1H_2O longitudinal relaxation rate constants) should be mapped and not simply assumed as they were here.
- Individual arterial input functions (AIFs) should be used if possible. A reference tissue method (30), or an automated AIF determination (ex., Jim 4.0 software; Xinapse Systems), could prove important in this regard.
- Increased temporal resolution should be achieved without sacrificing spatial resolution or signal-to-noise ratio. Parallel RF excitation/acquisition (31, 32) should be crucial. With good definition of the DCE time-course first-pass leading edge, the second-generation SSM [BALDERO (Blood Agent Level-Dependent and Extravasation Relaxation Overview)] analysis (which accounts for blood ^1H_2O signal pharmacokinetic behavior) can be used to also determine v_b and k_{bo} values (5). It is widely anticipated that tumor v_b values will have significant diagnostic value. Furthermore, $v_b k_{bo}$ is the transendothelial water permeability coefficient surface area product, $P_W S'$, where S' is the total capillary bed surface area. The ratio $P_W S'/P_{CR} S'$ would be the intensive property P_W/P_{CR}. The value of the CR permeability coefficient surface area product ($P_{CR} S'$) can be factored from the K^{trans} parameter using the blood flow value, which can also be determined from DCE-MRI data (17).
- The DCE-MRI pharmacokinetic images should be spatially registered to correct for patient motion.
- Image acquisition without -$^1CH_2$- suppression can yield signal intensities much more amenable to precision parametric mapping. The maps require sufficient acquisition contrast-to-noise ratio because pixel-by-pixel analytical modeling is more susceptible to noise. (The bulk of the image data here, obtained with –^1H_2C– signal suppression, has a signal-to-noise ratio less than one-third that with no fat suppression. Perhaps there is some collateral ^1H_2O suppression.) However, care must be taken to avoid contamination of ^1H_2O by unsuppressed -^1H_2C-.

Conclusions

If this SSM DCE-MRI pharmacokinetic screening approach had been an integral part of institutional protocols for this 22 patient

population, 13 "unnecessary" biopsy procedures (those returning benign pathology results) would have been avoided, even if all five B-5 patients were advanced to pathology. If SSM DCE-MRI was the determinant (Fig. 4), all 15 of the (unnecessary) biopsies (68% of all) would have been obviated, if their purposes were to rule out malignancies. We find it quite remarkable that the fundamental NMR shutter-speed phenomenon becomes significant for the vascular properties of precisely malignant breast tumors. If recent epidemiological evidence correlating (benign) biopsy with increased subsequent breast cancer rate (33) reflects causality, then DCE-MRI biopsy minimization will carry an even greater benefit. This far outweighs the tiny incidence [0.00045% of the >30 million patients who have received a particular, suspect CR (34)] of serious reaction to CR administration, and which correlates with preexisting kidney compromise. We expect the SSM to also significantly quantify the proven DCE-MRI ability to detect very early responses to anticancer therapeutic interventions with approved drugs (*16*) and in drug discovery (35, 36).

And the SSM has much more to teach us. Besides smaller studies of a number of other malignant tumors in animal and human hosts (12, 13, 15, 16), we have applied the SSM to data from normal skeletal (8, 15), nonskeletal (9, 15), and myocardial (17) musculature, myocardium in hyperemia (17), multiple sclerosis lesions in cerebral white matter (15), and the normal blood-brain barrier. We think the SSM offers the opportunity for general quantitative vascular phenotyping in vivo.

Materials and Methods

Details on some of the MRI data acquisitions and analyses have been published (14, 15), and more are found in ref. 18. Only aspects particular to the subjects are presented here.

Patients. A total of 22 patients was recruited from clinical breast cancer populations that had undergone initial screening steps at two different institutions. These comprised mammographic and/or clinical breast MRI protocols that included high spatial resolution pre-CR T_2-weighted and pre-CR and post-CR T_1-weighted acquisitions, and low-temporal-resolution DCE-MRI with fewer than eight time points. All had mammographic and/or CR-enhanced lesions radiologically classified in the B-4 (n = 17) or B-5 (n = 5) categories based on lesion morphology and/or qualitative assessment of enhancement kinetics (persistent, plateau, or washout) (19–22). These diagnoses led to biopsy referrals. The research DCE-MRI data acquisitions were performed under Institutional Review Board-approved protocols, and informed consent was obtained from each patient. The data from six patients, some of which have been published (14, 15), were collected in the MR Research Center of the Department of Radiology at the State University of New York at Stony Brook, as part of a combined MRI/MRS protocol (37) before excisional or core biopsy. Those from the other 16 patients were acquired at the Memorial Sloan-Kettering Cancer Center just before needle insertions in clinically scheduled MRI-guided preoperative needle localization or core biopsy procedures.

DCE-MRI Data Acquisition. The study was conducted by using two different 1.5-T MR systems [Edge (Philips/Marconi Medical Systems) at Stony Brook and Excite (General Electric) at Sloan Kettering] with body radio frequency transmitter coils, and four-channel (Stony Brook and Sloan Kettering) and seven-channel (Sloan Kettering) phased-array bilateral breast RF receiver coils, with compression plates, for the prone patient. Data acquisition details are given in ref. 18. Different CR molecules [GdDTPA-BMA (Gadodiamide, Omniscan; Nycomed) (Stony Brook); $GdDTPA^{2-}$ (Magnevist; Berlex) (Sloan Kettering)] were used.

DCE-MRI Pharmacokinetic Analyses. Considerable detail on this aspect is given in ref. 18.

ACKNOWLEDGMENTS. We thank Drs. Patricia Carney (for refs. 1, 24, and 33), Jeffrey Evelhoch (for ref. 35), Charles Thomas (for ref. 28), David Dawson, and Tanya Carter for important discussions; Charles Nyman and Thomas Mair for technical assistance; and Drs. Anuradha Khilnani, Ralph Wynn, Sandra Brennan, and Jennifer Kaplan for patient recruitment. This work was supported by National Institutes of Health Grants RO1 NS-40801 and RO1 EB-00422 (to C.S.S.) and RO1 CA-120861 (to W.H.), the W. M. Keck Foundation (C.S.S.), a State University of New York at Stony Brook–Brookhaven National Laboratory Seed Grant (to W.H. and C.S.S.), and a Memorial Sloan-Kettering Cancer Center Byrne Fund award (to W.H.).

1. Fenton JJ, *et al.* (2007) Influence of computer-aided detection on performance of screening mammography. *N Engl J Med* 356:1399–1409.
2. Saslow D, *et al.* (2007) American Cancer Society guidelines for breast screening with MRI as an adjunct to mammography. *CA Cancer J Clin* 57:75–89.
3. Lehman CD, *et al.* (2007) MRI evaluation of the contralateral breast in women with recently diagnosed breast cancer. *N Engl J Med* 356:1295–1303.
4. Tofts PS, *et al.* (1999) Estimating kinetic parameters from dynamic contrast-enhanced T_1-weighted MRI of a diffusable tracer: Standardized quantities and symbols. *J Magn Reson Imaging* 10:223–232.
5. Li X, Rooney WD, Springer CS (2005) A unified magnetic resonance imaging pharmacokinetic theory: Intravascular and extracellular contrast reagents. *Magn Reson Med* 54:1351–1359 and erratum (2006) 55:1217.
6. Labadie C, Lee J-H, Vétek G, Springer CS (1994) Relaxographic imaging. *J Magn Reson B* 105:99–112.
7. Donahue KM, Weisskoff RM, Burstein D (1997) Water diffusion and exchange as they influence contrast enhancement. *J Magn Reson Imaging* 7:102–110.
8. Landis CS, *et al.* (1999) Equilibrium transcytolemmal water–exchange kinetics in skeletal muscle *in vivo*. *Magn Reson Med* 42:467–478.
9. Landis CS, *et al.* (2000) Determination of the MRI contrast agent concentration time course *in vivo* following bolus injection: Effect of equilibrium transcytolemmal water exchange. *Magn Reson Med* 44:563–574.
10. Springer CS, Rooney WD, Li X (2002) The effects of equilibrium transcytolemmal water exchange on the determination of contrast reagent concentration *in vivo*. *Magn Reson Med* 47:422–424.
11. Quirk JD, *et al.* (2003) Equilibrium water exchange between the intra- and extracellular spaces of mammalian brain. *Magn Reson Med* 50:493–499.
12. Yankeelov TE, Rooney WD, Li X, Springer CS (2003) Variation of the relaxographic ''shutter-speed'' for transcytolemmal water exchange affects the CR bolus-tracking curve shape. *Magn Reson Med* 50:1151–1169.
13. Zhou R, Pickup S, Yankeelov TE, Springer CS, Glickson JD (2004) Simultaneous measurement of arterial input function and tumor pharmacokinetics in mice by dynamic contrast enhanced imaging: Effects of transcytolemmal water exchange. *Magn Reson Med* 52:248–257.
14. Li X, *et al.* (2005) Shutter-speed analysis of contrast reagent bolus-tracking data: Preliminary observations in benign and malignant breast disease. *Magn Reson Med* 53:724–729.
15. Yankeelov TE, *et al.* (2005) Evidence for shutter-speed variaton in CR bolus-tracking studies of human pathology. *NMR Biomed* 18:173–185.
16. Chang EY, *et al.* (2008) The evaluation of esophageal adenocarcinoma using dynamic contrast enhanced magnetic resonance imaging. *J Gastrointestinal Surg* 12:166–175.
17. Li X, Springer CS, Jerosch-Herold M (2008) First-pass DCR-MRI with extravasating CR: Evidence for human myocardial capillary recruitment in adenosine-induced hyperemia. *NMR Biomed*, 10.1002/nbm.1293.
18. Li X, *et al.* (2008) Dynamic NMR effects in dynamic-contrast-enhanced MRI of breast cancer. *Proc Natl Acad Sci USA*, 10.1073/pnas.0804224.
19. Tofts PS, Berkowitz B, Schnall MD (1995) Quantitative analysis of dynamic Gd-DTPA enhancement in breast tumors using a permeability model. *Magn Reson Med* 33:564–568.
20. Buadu LD, *et al.* (1996) Breast lesions: Correlation of the contrast medium enhancement patterns on MR images with histopathologic findings and tumor angiogenesis. *Radiology* 200:639–649.
21. Degani H, Gusis V, Weinstein D, Fields S, Strano S (1997) Mapping pathophysiological features of breast tumors by MRI at high spatial resolution. *Nat Med* 3:780–782.
22. Daniel BL, *et al.* (1998) Breast disease: Dynamic spiral MR imaging. *Radiology* 209:499–509.
23. Salter JT, Miller KD (2007) Antiangiogenic agents in breast cancer. *Cancer Invest* 25:518–526.
24. Poplack SP, *et al.* (2005) Screening mammography: Costs and use of screening-related services. *Radiology* 234:79–85.
25. Huang W, *et al.* (2007) Shutter-speed DCE-MRI pharmacokinetic analyses facilitate the discrimination of malignant and benign breast disease. *Proc Int Soc Magn Reson Med* 15:141.
26. Schabel M, Morrell G (2007) Dynamic contrast-enhanced MRI for breast cancer detection. *Proc Int Soc Magn Reson Med* 15:2945.
27. Li CI, Malone KE, Saltzman BS, Daling JR(2006) Risk of invasive breast carcinoma among women diagnosed with ductal carcinoma *in situ* and lobular carcinoma *in situ*, 1988–2001. *Cancer* 106:2104–2112.
28. Kuhl CK, *et al.* (2007) MRI for diagnosis of pure ductal carcinoma *in situ*: A prospective observational study. *Lancet* 370:485–492.
29. Kim YR, Rebro KJ, Schmainda KM (2002) Water exchange and inflow affect the accuracy of T_1-GRE blood volume measurements: Implications for the evaluation of tumor angiogenesis. *Magn Reson Med* 47:1110–1120.
30. Yang C, Karczmar GS, Medved M, Stadler WM (2004) Estimating the arterial input function using two reference tissues in dynamic contrast-enhanced MRI studies: Fundamental concepts and simulations. *Magn Reson Med* 52:1110–1117.
31. Tozaki M, Fukuda M (2006) Supine MR mammography using VIBE with parallel acquisition technique for the planning of breast-conserving surgery: Clinical feasibility. *Breast* 15:137–140.
32. Dougherty L, *et al.* (2007) High frame-rate simultaneous bilateral breast DCE-MRI. *Magn Reson Med* 57:220–225.
33. Ashbeck EL, Rosenberg RD, Stauber PM, Key CR (2007) Benign breast biopsy diagnosis and subsequent risk of breast cancer. *Cancer Epidemiol Biomarkers Prev* 16:467–472.
34. Thomsen HS (2006) Nephrogenic systemic fibrosis: A serious late adverse reaction to gadodiamide. *Eur Radiol* 16:2619–2621.
35. Liu G, *et al.* (2005) Dynamic contrast-enhanced magnetic resonance imaging as a pharmacodynamic measure of response after acute dosing of AG-013736, an oral angiogenesis inhibitor, in patients with advanced solid tumors: Results from a phase I study. *J Clin Oncol* 23:5464–5473.
36. Galbraith SM (2006) MR in oncology drug development. *NMR Biomed* 19:681–689.
37. Huang W, *et al.* (2004) Detection of breast malignancy: Diagnostic MR protocol for improved specificity. *Radiology* 232:585–591.